ENGINEERING

Exploiting multiscale dynamic toughening in multicomponent alloy metamaterials for extreme impact mitigation

James U. Surjadi[1,2,3]†, Liqiang Wang[1,4]†, Shuo Qu[4], Bastien F.G. Aymon[3], Junhao Ding[4], Xin Zhou[1,5], Rong Fan[1], Hui Yang[6], Qi Zhao[6], Xu Song[4]*, Yang Lu[1,2,7,8]*

Mechanical metamaterials can unlock extreme properties by leveraging lightweight structural design principles and unique deformation mechanisms. However, research has predominantly focused on their quasi-static characteristics, leaving their behavior under extreme dynamic conditions, especially at length scales relevant to practical applications largely unexplored. Here, we present a strategy to achieve extreme impact mitigation at the macroscale by combining shell-based microarchitecture with an additively manufactured medium-entropy alloy (MEA) featuring low stacking fault energy (SFE). Notably, the shell-based architecture amplifies the effective dynamic stress within the metamaterial compared to truss-based morphologies, leading to the earlier activation of multiscale toughening mechanisms in the alloy. The low SFE of the MEA enables the evolution of a diverse array of defect types, thereby prolonging strain hardening behavior across seven orders of magnitude in strain rate. These fundamental insights could establish the groundwork for developing scalable, lightweight, impact-resistant metamaterials for structural and defense applications.

INTRODUCTION

From woodpecker beaks to everyday foam packaging, lightweight cellular materials have played an indispensable role in protective systems for centuries due to their ability to effectively dissipate impact energy (*1*). Yet, their stochastic nature restricts tunability in their mechanical response, imposing an upper bound on their energy dissipation capabilities. The advent of additive manufacturing (AM), commonly referred to as three-dimensional (3D) printing, has provided (1) unprecedented freedom in manufacturing parts with complex geometries and distinct microstructures, and (2) direct usability, allowing the manufacture of ready-to-use parts with little to no post-processing, unlike traditional manufacturing where casting or machining is required for shaping. Consequently, mechanical metamaterials, which are essentially topologically engineered 3D architectures (often manufactured via AM processes), have emerged as a premium lightweighting and toughening strategy over conventional stochastic foams or aerogels (*2*–*4*). Particularly, metallic lattices have garnered substantial attention due to their ability to combine metal/alloy toughening mechanisms with stiff and strong architectures, achieving remarkable combinations of low density, high strength, and energy dissipation (*5*–*9*). However, existing studies on mechanical metamaterials have primarily focused on characterizing quasi-static properties with small number of tessellations, restricting the full potential of these materials system from being harnessed.

Prior investigations on the dynamic properties of metamaterials have illuminated the ability of tailored architectures to elicit energy dissipation mechanisms, such as compaction fronts and multistability (*10*–*14*). Recently, by exploiting nanomechanical size effects enabled by nanoscale AM (i.e., two-photon polymerization), pyrolytic carbon nanolattices have demonstrated unprecedented impact energy dissipation, outperforming commonly-used impact-resistant materials such as steel and Kevlar (*15*). Nevertheless, the current throughput of nanoscale AM processes makes it challenging to scale up submicron feature sizes to macroscale samples within the timeframes required for practical applications, such as lightweight armors, satellites, and vehicles. Therefore, there is an urgent need to develop metamaterials that can achieve comparable performance to nanoscale metamaterials while also being scalable to meter-scale dimensions.

In recent years, multicomponent alloys such as high- and medium-entropy alloys (HEA/MEAs) that are composed of multiple principal elements often at near equiatomic ratios have been reported to exhibit superior mechanical and functional properties compared to traditional alloys (*16*). For instance, CoCrNi MEA is one of the toughest materials known to date due to its low stacking fault energy (SFE), giving rise to a continuous sequence of toughening mechanisms that prolong strain hardening behavior even under extreme cryogenic and dynamic loading conditions (*17*, *18*). Despite notable progress, innovations in HEA/MEAs have primarily focused on developing new alloy compositions or processing methods to alter the microstructure and mechanical properties of bulk/monolithic components with relatively simple geometries (*16*). Explorations on 3D architected HEA/MEAs have been scarce, with existing reports focusing solely on quasi-static mechanical properties and thus hindering their translation into real-world scenarios (*19*–*25*).

In this work, via a self-developed high-resolution selective laser melting (HR-SLM) system, we fabricated lightweight CoCrNi

[1]Department of Mechanical Engineering, City University of Hong Kong, Kowloon, Hong Kong SAR, China. [2]Hong Kong Institute for Advanced Study, City University of Hong Kong, Kowloon, Hong Kong SAR, China. [3]Department of Mechanical Engineering, Massachusetts Institute of Technology, Cambridge, MA, USA. [4]Department of Mechanical and Automation Engineering, Chinese University of Hong Kong, Shatin, Hong Kong, China. [5]Physikalisches Institut, Westfälische Wilhelms-Universität, Münster 48149, Germany. [6]Department of Civil and Environmental Engineering, The Hong Kong Polytechnic University, Hung Hom, Kowloon, Hong Kong, China. [7]Nano-Manufacturing Laboratory (NML), Shenzhen Research Institute of City University of Hong Kong, Shenzhen, China. [8]Department of Mechanical Engineering, The University of Hong Kong, Pokfulam, Hong Kong.
*Corresponding author. Email: xsong@mae.cuhk.edu.hk (X.S.); ylu1@hku.hk (Y.L.)
†These authors contributed equally to this work.

MEA micro-architected metamaterials with ultrahigh-energy dissipation across a wide range of strain rates (spanning over seven orders of magnitude), surpassing existing metamaterials/alloys. We also provide the foundation to bridge the gap between two previously independent concepts, 3D metamaterials under impact and extreme dynamic toughening in additively manufactured multicomponent alloys. Postmortem micro–computed tomography (μCT) reconstruction, electron backscatter diffraction (EBSD), high-resolution transmission electron microscopy (HRTEM), and finite element analysis (FEA) reveal a synergistic interplay between the energy dissipation mechanisms inherent to the HR-SLM MEA and the metamaterial architecture. Specifically, triply periodic minimal surface (TPMS)–based architectures exhibit a more pronounced inertial response under dynamic loading compared to truss-based architectures. This results in enhanced dynamic stress at a given strain rate, leading to the earlier activation of toughening mechanisms within the low SFE alloy. Our study not only demonstrates the potential of shell-based, microarchitected multicomponent alloys as high-performance, impact-resistant materials with macroscale sample sizes but also provides mechanistic insights into the sparsely explored dynamic regime. These insights could contribute to establishing design parameters for next-generation lightweight, mechanically robust mechanical metamaterials across various strain rates.

RESULTS

HR-SLM and quasi-static mechanical properties

An in-house developed HR-SLM system was used to fabricate the CoCrNi MEA 3D microarchitected metamaterials (Fig. 1A). This system is based on the principle of 3D layer-by-layer melting of metal powders using continuous-wave Nd:yttrium-aluminum-garnet laser. Unlike commercially available systems (laser spot size, 50 to 100 μm; and slicing distance, 20 to 100 μm), the HR-SLM system achieves superior precision with a smaller spot size of 25 μm and layer thickness of 10 μm (Fig. 1B). The custom-made laser optics system plays a key role in enlarging the incident laser's diameter at the source, thereby reducing the final laser spot size to 25 μm through the f-theta lens (table S1). In addition, the thinner layer thickness can be ascribed to the use of finer powder sizes and a specialized recoater design (table S2 and fig. S1). The HR-SLM process induces a finer grain structure and a denser dislocation cell network in the printed parts compared to conventional SLM techniques (fig. S2 and table S3). This refined microstructure has been previously associated with increased strength without compromising ductility (Fig. 1, B and C) (*26*). The reduced laser beam size in our modified SLM process plays a key role in achieving these improvements by enabling finer control over the thermal gradient and cooling rate. In addition, other factors contribute as well, including optimized scan strategies, adjusted laser power, and the tailored physical properties of the feedstock, which are shown in detail in fig. S4 and table S5. All the samples used for quasi-static and dynamic impact experiments (Fig. 1D) are fabricated using optimized printing parameters (volume energy density, ~125 J mm^{-3}) and post-treatment conditions (texts S1 and S2).

Three representative types of 3D architectures at similar relative densities (~17%) were investigated in this study, (i) bending-dominated body-centered cubic (BCC) strut lattice, (ii) stretching-dominated strut lattice (octet) (*27*), a widely studied lattice architecture known for their high specific strength, and (iii) stretching-dominated TPMS shell lattice (gyroid) (*28*). Quasi-static in situ uniaxial compression of the MEA microlattices up to 60% strain (near their densification strains) exhibit ductile deformation behaviors via layer-by-layer buckling of its struts/shells with little to no fracture and apparent shear banding (Fig. 2A). The corresponding stress-strain curves show that while the octet-truss microlattice can attain higher modulus and strength (over two times that of BCC), postyield softening and fluctuations in the stress-strain curve results in a nonideal energy absorption response (only ~45% higher than BCC) (*29*). In contrast, the gyroid shell microlattice not only exhibits superior mechanical properties (over four times higher modulus and strength than BCC), but also displays a smoother stress-strain curve than the octet-truss with no postyield softening, resulting in over two times higher specific energy absorption (Fig. 2B).

FEA was performed to further analyze the origins of enhanced mechanical properties of the gyroid shell microlattice compared to the strut microlattices. The elastic surface of the gyroid shell architecture encompasses entirely those of both the octet and BCC structures (Fig. 2C). This observation confirms that, in all directions, the gyroid exhibits greater stiffness compared to an equally dense periodic truss lattice, thus supporting the experimental findings. Nonlinear simulations, incorporating plasticity, were performed to investigate the underlying factors contributing to the superior strength and energy absorption of the gyroid in comparison to the octet and BCC lattices. The maximum principal strain contour of the gyroid lattice demonstrates more uniform strain distribution compared to the octet and BCC lattices where deformation is concentrated at the nodes (fig. S11A), primarily due to its continuous and smooth surface topology with zero mean curvature. This geometric efficiency minimizes stress concentration and redistributes deformation more evenly across the structure (fig. S11B), resulting in higher average equivalent plastic strain, as shown in the simulation results (fig. S11C). For the gyroid lattice, the higher average equivalent plastic strain value observed in the simulation reflects its ability to achieve higher strength and dissipate more energy plastically at a given compressive strain compared to the truss-based lattices. The enhanced plastic dissipation for the gyroid contributes to its superior strength and energy dissipation, accentuated by the intrinsically ductile response of the MEA (Fig. 2D). It is imperative to recognize that the drastic improvement in the mechanical performance of the shell microlattice over truss microlattices is only made possible due to the ideal combination of architectural features with the intrinsic characteristics of its constituents. For instance, Ti-6Al-4V gyroid shell lattices exhibit a brittle behavior, with numerous shell fractures and distinct shear bands represented by the drastic stress drop (>60%) upon yielding (*30*). Such brittleness limits the full utilization of the shell architecture in terms of its energy absorption behavior. Hence, the high strength and ductility of the HR-SLM MEA are pivotal for achieving optimal mechanical performance.

In situ projectile impact and architecture-induced dynamic effects

To investigate the extreme dynamic response of the HR-SLM MEA microlattices, a series of in situ projectile impact tests were conducted over a range of velocities from 100 to 1500 m s^{-1} (Fig. 3).

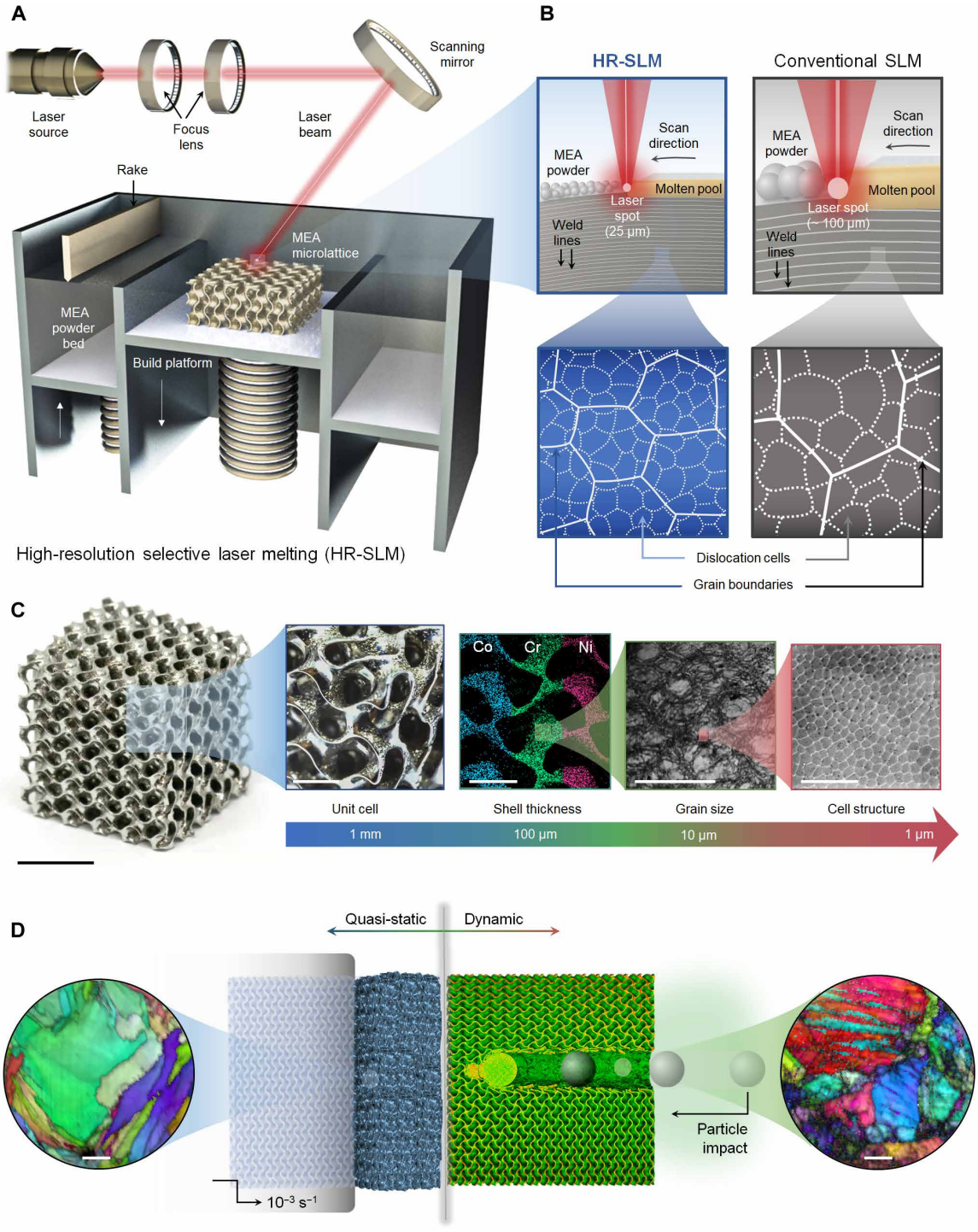

Fig. 1. Fabrication and multiscale characterization of HR-SLM MEA microlattices across various strain rates. (**A**) Schematic of the HR-SLM system used to fabricate the MEA microlattices. (**B**) Illustration comparing our HR-SLM system with conventional, commercially available SLM systems in terms of their printing configuration and resulting microstructures, in particular dislocation cell density. (**C**) Hierarchical structure of the MEA shell microlattice showing the sub–100-μm shell thickness of the gyroid microlattice overlapped with energy-dispersive x-ray (EDX) mapping of its composition, grain boundaries of the HR-SLM MEA obtained via electron backscatter diffraction image quality map (EBSD-IQ), and dense, nanoscale dislocation cell network induced by HR-SLM. Scale bars, 5 mm (overall sample), 1 mm (unit cell), 1 mm (shell thickness), 100 μm (grain size), and 2 μm (cell structure). (**D**) Postmortem images of deformed MEA microlattices, showing the difference in microstructure when subjected to quasi-static or dynamic loading. Scale bars, 10 μm.

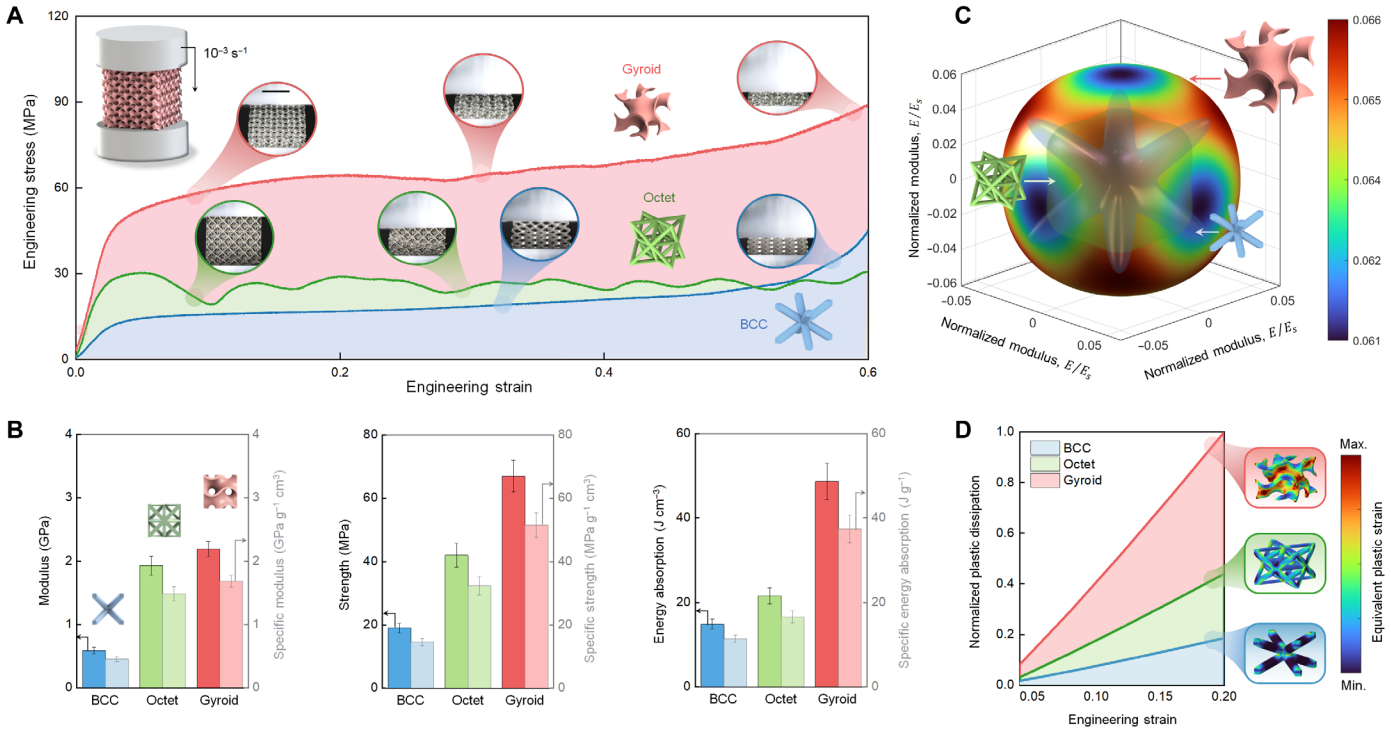

Fig. 2. Quasi-static mechanical characterization of HR-SLM MEA microlattices. (**A**) In situ uniaxial compression of MEA microlattices and the corresponding engineering stress-strain curves. Scale bar, 5 mm. (**B**) Plots comparing the absolute and density-normalized (specific) Young's modulus, yield strength, and energy absorption (defined as the area under stress-strain curve) of the MEA microlattices under compression. (**C**) Elastic surfaces of the BCC, octet, and gyroid architectures. The elastic surfaces of the gyroid encompass the elastic surfaces of both the BCC and octet architectures, indicating that the gyroid is stiffer in all directions. The normalized modulus represents the modulus of the lattices normalized against the modulus of its constituent material. (**D**) Normalized total plastic dissipation of the BCC, octet, and gyroid architectures upon yielding, showing that stretching-dominated architectures, in particular gyroid, dissipate more energy plastically at a given strain. The plastic dissipation values are normalized against the dissipation value of the gyroid to show the relative difference across architectures.

In this setup, a stainless-steel sphere was accelerated using a gas gun, and a high-speed camera was used to observe the impact event (fig. S12). Notably, the projectiles fully penetrated the samples of the BCC and octet lattices at velocities surpassing 500 m s^{-1} (figs. S13 and S14). In contrast, the gyroid lattice managed to arrest the projectile, preventing complete penetration even at velocities exceeding 900 m s^{-1} (Fig. 3A). This signifies a pivotal difference in their impact resistance and energy absorption capabilities despite all samples having a similar mass. A comparison of the specific inelastic energy of the MEA microlattices, defined as the total dissipated energy normalized by the participating material mass within the crater (*15*, *31*), reveals a substantial superiority of the gyroid shell architecture over the truss-based BCC and octet architectures (Fig. 3B). Despite a clear difference in the energy dissipated by the BCC and octet lattices under quasi-static loading, there is minimal disparity in their specific inelastic energy values during dynamic loading. The BCC lattices even marginally outperform the octet lattices at low projectile impact velocities (100 to 200 m s^{-1}), which is atypical to previous findings, where strength typically played a dominant role in dictating dynamic energy dissipation (*15*, *32*, *33*).

Postmortem μCT reconstruction and dynamic explicit FEA were used to elucidate the mechanisms contributing to the divergence in the mechanical properties of the MEA microlattices under quasi-static and dynamic loading conditions. Cross-sectional morphologies of the impacted samples revealed localized fracture surfaces for all architectures (Fig. 3C) (*15*, *31*), indicative of effective shock mitigation and force attenuation, as discernible damage was confined to the impact region. Further examination of the compaction fronts unveiled a distinctive characteristic of the gyroid shell lattice; its compaction front appears to be of greater density compared to the octet truss lattice (Fig. 3D). 3D μCT reconstructions of the gyroid lattices impacted at different strain rates (fig. S15) confirmed that the dense region beneath the projectile was not a tomography artifact but rather a direct consequence of the lattice's deformation. FEA of the compaction event substantiated these observations (Fig. 3E). Specifically, as the gyroid lattice compacts, each shell layer folds neatly onto itself, forming a dense region beneath the projectile, an effect corroborated by finite element simulations (fig. S16). The notable similarity between the simulated and experimental compaction fronts further supports this finding (fig. S17). In contrast, the octet truss lattice develops a more fragmented and disordered compaction front due to stress concentrations at the nodes, resulting in higher porosity and a reduced contact area at the impact site (Fig. 3F and fig. S18). This larger contact area enables more material to actively participate in energy absorption, leading to greater plastic dissipation (Fig. 3G). Notably, the BCC lattice also displayed a larger contact area and greater plastic dissipation than the octet lattice upon compaction, explaining its marginally higher energy dissipation at lower velocities.

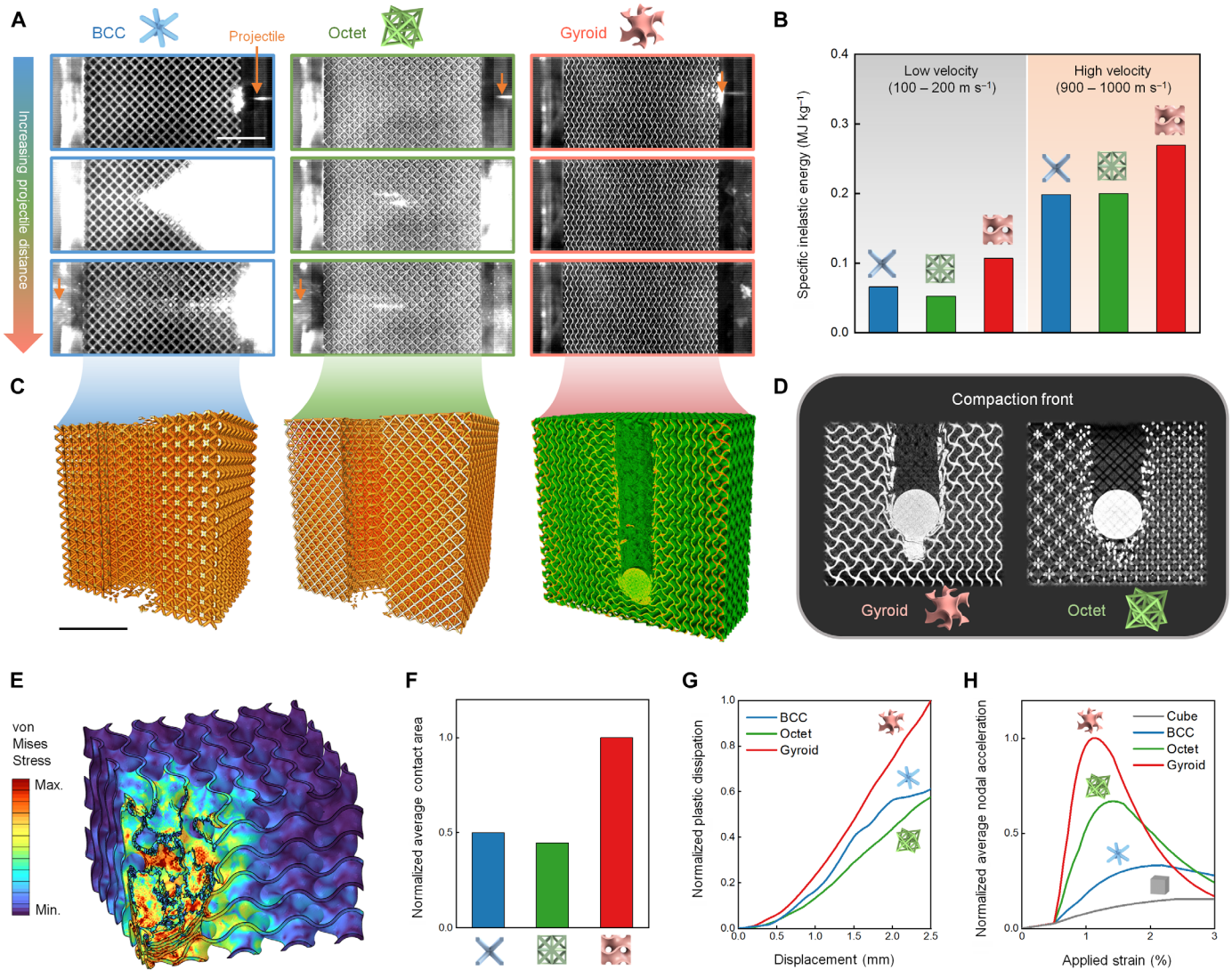

Fig. 3. Dynamic testing and architecture-induced dynamic toughening. (**A**) Snapshots of ballistic impact tests on HR-SLM MEA microlattices at an initial projectile velocity of ~900 ms^{-1}, showing that the projectile fully penetrates the truss BCC and octet lattices, but not the shell gyroid lattice. (**B**) Comparison of the specific inelastic energy dissipated by the MEA microlattices at low and high impact velocities. (**C**) Postmortem μCT 3D reconstruction of the MEA microlattices upon impact at projectile velocity of ~900 ms^{-1}. (**D**) Cross-sectional μCT scan of the compaction front of the gyroid and octet microlattices upon compaction, demonstrating the higher compaction density (larger self-contact area) of the gyroid compared to the octet. (**E**) Von Mises stress contour of the compaction event for a gyroid lattice. (**F**) Contact area underneath the impact upon compaction normalized by the contact area for the gyroid lattice, showing the relative difference in the amount of self-contact in the compaction regime. (**G**) Comparison of the relative plastic energy dissipation of the different architectures upon compaction. (**H**) Volume-averaged nodal acceleration normalized by element volume for different lattice architectures and monolithic cube of the same nominal dimensions upon dynamic loading. Higher peak average nodal acceleration implies larger inertial response, which enhances dynamic stress within the metamaterial. Scale bars, 10 mm.

Conversely, the octet lattice experience higher volume-averaged nodal acceleration than the BCC lattice (Fig. 3H and fig. S19), suggesting a more pronounced inertial response or "kickback" attributable to dynamic loading (*34*). The enhanced inertial response effectively increases the dynamic stress experienced by the metamaterial, thereby amplifying any strain rate–dependent material response (*34*). This finding is of notable importance, especially in the context of recent reports suggesting that elevated strain rates can instigate additional deformation mechanisms in multicomponent alloys, consequently increasing the inherent material toughness (*18*, *35*). The increasing dominance of inertial effects at elevated strain rates provide insight into the observed phenomenon where the octet lattice slightly outperforms the BCC lattices at dissipating energy in the high-velocity regimes (Fig. 3B and table S8).

The influence of projectile sizes relative to sample size was also investigated. When the projectile diameter was increased from 5 to 10 mm for a projectile traveling at approximately 900 m s^{-1} (fig. S20), the BCC lattice outperformed the octet lattice in terms of its specific inelastic energy. This occurs because the contact area and plastic dissipation in the compacted region are considerably larger for the BCC lattice. At higher velocities, where the octet lattice previously slightly outperformed the BCC lattice with a 5 mm projectile

due to higher induced dynamic stress effects, the larger projectile size shifted the dominant factor to compaction. Specifically, when the projectile diameter is equivalent to or exceeding five unit cells, compaction dominates, whereas inertial response is more dominant when the projectile is smaller. Simulation results further demonstrate this trend: At larger projectile sizes, the differences in contact area in the compaction regime and plastic dissipation are more pronounced between the BCC and octet lattices (fig. S21). However, the gyroid consistently outperforms both strut-based lattices across all regimes due to its superiority in both its compaction morphology and induced dynamic stress.

Overall, the gyroid shell lattice stood out in this study, demonstrating the highest inertial response (average nodal acceleration) under dynamic loading and plastic dissipation under compaction, resulting in superior dynamic energy dissipation capabilities. It is crucial to note that the potential competition between architecture-induced dynamic energy dissipation mechanisms essentially divides the dynamic performance of metamaterials into two regimes: (i) the low-velocity regime where energy dissipation upon compaction dominates and (ii) high-velocity regime where inertial response that can elevate the dynamic stress within the material dominates. In our study, for a projectile with diameter less than three unit cells wide, this transition from compaction-dominated regime to inertia-dominated regime seems to occur at projectile velocities in the range of 300 to 500 ms^{-1} (table S8). However, the transition point between the two regimes can be influenced by factors such as projectile size, which enhances the influence of compaction. For instance, the influence of compaction still dominates even at projectile velocities exceeding 900 m s^{-1} when the diameter of the projectile was increased to five unit cells wide (fig. S21). Furthermore, the multiscale coupling between the architecture and constituent material response requires a comprehensive understanding of both architecture- and material-induced mechanisms, including their interactions, to manufacture metamaterials with optimal dynamic response. Specifically, the heightened inertial response resulting from the gyroid shell architecture could prove disadvantageous for energy dissipation if constructed from a material prone to increased brittleness at higher strain rates (*36*), underscoring the necessity for selecting the ideal combination of metamaterial architecture and strain rate–dependent material characteristics.

Multiscale dynamic toughening in HR-SLM CoCrNi

Despite the recent interest on understanding the deformation mechanisms of HEA/MEAs under dynamic loading (*18*, *35*), the observed variance in inertial response between a monolithic component and a microlattice (Fig. 3H) implies that it is inadequate to extrapolate dynamic deformation mechanisms of a microlattice from the characterization of a monolithic material. Furthermore, existing reports on the dynamic response of HEA/MEAs have mainly focused on samples produced via traditional manufacturing methods (*37*). Hence, the influence of AM-induced microstructures (*26*, *38*–*40*), such as dislocation cells (*26*), and 3D architecture on the mechanical response across a spectrum of strain rates have remained largely unexplored. To gain mechanistic insights into the dynamic deformation mechanisms of the HR-SLM CoCrNi MEA (the detailed microstructure of the undeformed sample is provided in fig. S22 for comparison), postmortem EBSD and TEM images were obtained from the craters of the gyroid lattices (fig. S23) impacted at various strain rates/velocities, as shown in Fig. 4. Note that while different lattice architectures can influence the local strain distribution during impact, the differences in the microstructure are not drastic enough to alter the overall deformation mechanism.

In the quasi-static or weakly dynamic regime (strain rates below 10^3 s^{-1}), the primary deformation mechanism in our HR-SLM MEA stems from the interplay between deformation twins (DTs) induced by the low SFE (~20 mJ mm^{-2}) of CoCrNi (*17*, *41*) and dislocation cell network (Fig. 4, A to C) (*42*, *43*). During the printing process, the highly localized melting and rapid solidification generates large thermal gradients that induce multiaxial thermal stress within the microscale melt pool, resulting in the formation of nonequilibrium microstructures such as dislocation cells that are unachievable through conventional solidification processes (*41*, *42*). At the initial stages of deformation, the presence of a network structure of dislocation cells hinders dislocation mobility, leading to the accumulation of dislocations at cell walls and consequently enhancing yield strength (*44*–*46*). Unlike other strengthening mechanisms that often compromise ductility, partial dislocations can still traverse dislocation cell walls, enabling continuous and stable plastic flow even under elevated stress levels (*44*). Subsequent deformation results in elongated dislocation cells along the shear stress direction and thin (a few atomic layers) DTs on {111} planes that penetrate dislocation cell walls but are eventually obstructed by high-angle grain boundaries (HAGBs) (Fig. 4, B and C). These findings underscore the crucial role of dislocation cell-DT-HAGB interactions in dissipating impact energy in MEA microlattices within the weakly dynamic regime.

As the nominal strain rate approached 10^3 s^{-1}, the heightened strain rate and inherent low SFE of CoCrNi MEA led to a considerable increase in the rate of defect accumulation, surpassing the annihilation process (*41*). This phenomenon manifested in the sustained nucleation and growth of DT structures, transforming the twin-twin network into a more intricate hierarchical defect microstructure. A densely distributed, thicker (approximately 50 nm), and hierarchical DT network, featuring abundant secondary and even tertiary twins, was consistently observed throughout the grains (Fig. 4, D and E). High-resolution TEM (Fig. 4F) unveils the interaction of triple twinning systems oriented in the same plane, with angles between them measuring approximately 70°. This intricate twining network can proliferate in multiple directions and interact with dislocations, producing a 3D defect network that extends strain hardening at high stress levels, thereby elevating both strength and ductility (*47*).

Further increasing the nominal strain rate to 10^4 s^{-1} resulted in the generation of complex DT networks with hexagonal close-packed (HCP) phase (fig. S24) and nanoscale amorphous bands in the shear-localized regions (Fig. 4, G and H), as evidenced by the apparent interface region between face-centered cubic (FCC) matrix and amorphous bands (Fig. 4I). Intriguingly, HCP-induced strain hardening and amorphization in HEA/MEAs have only been observed under extreme strain rates surpassing 10^5 s^{-1} (*18*, *35*). However, in our HR-SLM MEA microlattice, these phenomena were observed at lower strain rates, implying that 3D architecture and HR-SLM–induced artifacts may accelerate the activation of dynamic energy dissipation mechanisms. The formation of amorphous bands is linked to the drastic release of deviatoric stresses within defect-rich regions, impeding crack initiation and propagation (*35*). Moreover, the interfaces between amorphous and crystalline regions serve as nucleation sites and natural sinks for dislocations (*48*), effectively mitigating stress concentration and providing an additional energy dissipation mechanism.

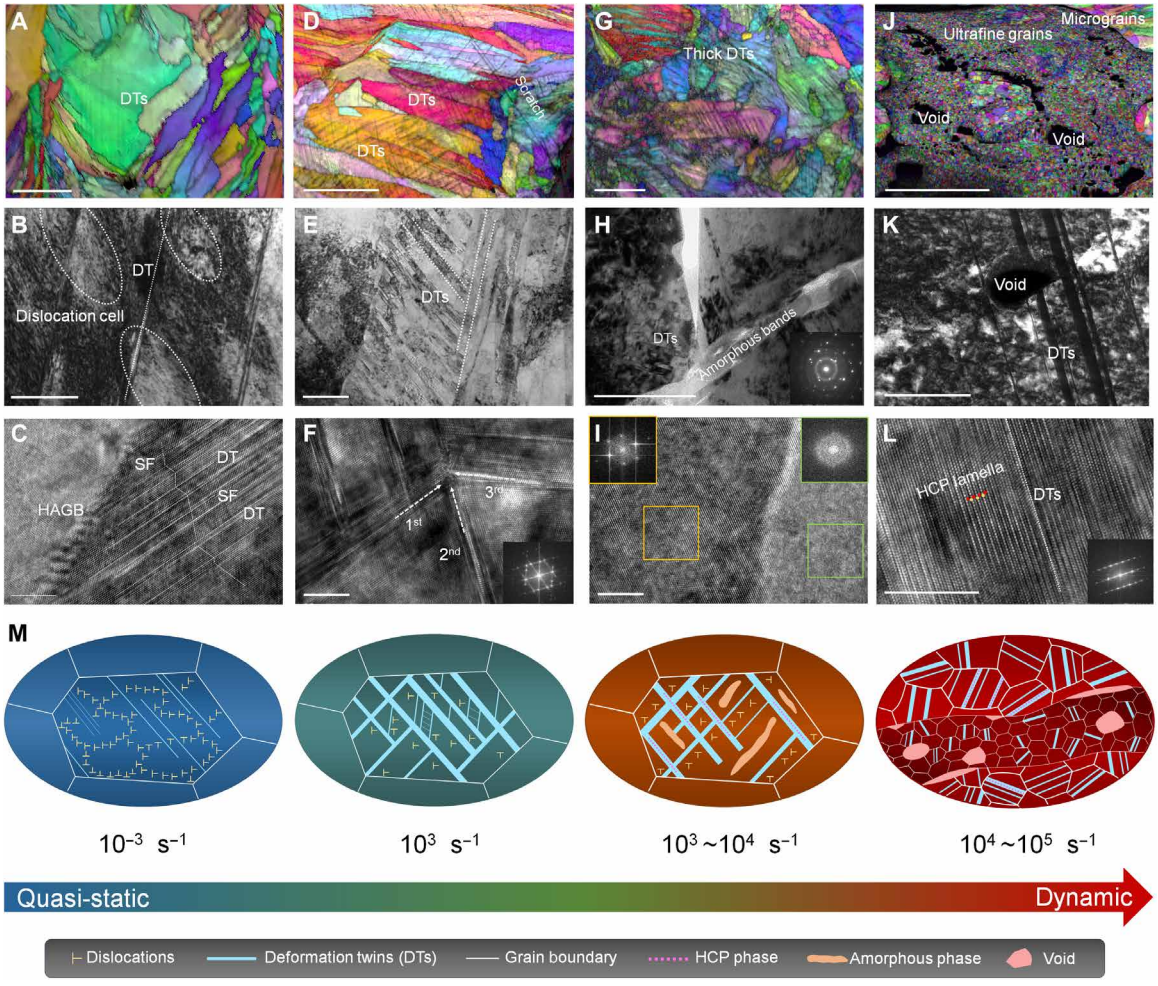

Fig. 4. Hierarchical deformation mechanisms of the CoCrNi MEA microlattices at different strain rates. (A to C) Quasi-static deformed microstructure in microlattice at the densification strain. (**A**) Inverse pole figure mapping (EBSD-IPF) showing the formation of thin DTs and (**B**) the corresponding bright field TEM image showing the intersections of DTs with the walls of dislocation cells. (**C**) HRTEM image showing the interaction behavior between parallel DTs and high-angle grain boundaries (HAGBs). (D to F) Deformed microstructure at nominal strain rate ~1000 s^{-1}. (**D**) EBSD-IPF showing the thick DTs. (**E**) TEM image demonstrating the hierarchical deformation twinning networks with abundant secondary twins and even tertiary twins. (**F**) The interaction behavior of triple deformation twinning systems and corresponding FFT pattern. (G to I) Deformed microstructure at nominal strain rate ~30,000 s^{-1}. (**G**) EBSD-IPF image showing the high-density and intricate network of DTs. (**H**) Nanosized amorphous bands. (**I**) Sharp interface between FCC matrix and amorphous bands, and corresponding FFT patterns. (J to L) Deformed microstructure at nominal strain rate ~50,000 s^{-1}. (**J**) Void and ultrafine equiaxed grains inside the ASBs. (**K**) Dark-field TEM image showing the DTs blocking the growth of voids. (**L**) HRTEM showing the HCP nanolamellas. Scale bars, (A, D, G, and J) 20 μm, (B, E, and H) 200 nm, (K) 100 nm, and (C, F, I, and L) 5 nm. (**M**) Schematic illustrations showing the deformation mechanism evolution with increased strain rates.

Adiabatic shear bands (ASBs) and restricted void nucleation were subsequently observed when the strain rate approaches 10^5 s^{-1} (fig. S25). At these extreme strain rates, the localized shear strain may result in a sudden and substantial temperature rise that drives the formation of ASBs, as the thermal softening effect surpasses strain rate hardening effects (*49*). This results in ultrafast quenching rates within the ASB, promoting dynamic recrystallization behavior (Fig. 4J and fig. S26) that yields ultrafine equiaxed grains devoid of pronounced texture, with an average grain size measuring approximately 300 nm (*50*). In addition, homogeneous nucleation of spherical microvoids was observed at multiple locations (fig. S27). The surrounding high-density defect network, such as the DTs with HCP nanolamellas, effectively hinders the void growth and coalescence (Fig. 4, K and L), thus delaying the formation of large cracks, which enhance the spall strength and damage tolerance of the MEA under extreme impact loading (*51*).

Overall, throughout the impact process at varying strain rates, the combination of HR-SLM artifacts and low SFE of the MEA resulted in an extensive array of defect types and dynamic evolution patterns, encompassing distorted dislocation cells, highly activated multiple DTs, hexagonal nanolamellas, nanosized amorphous bands, and restricted void nucleation (Fig. 4M). This intricate evolution of defect variations and deformation mechanisms facilitate hierarchical energy dissipation at varying stress levels, thereby preventing catastrophic crack growth and contributing to the effective reinforcement of the material under extreme dynamic loading conditions.

Performance comparison

The mechanical performance of HR-SLM MEA shell microlattices is systematically compared with other reported microlattices and metallic materials, focusing on specific compressive strength and energy absorption capabilities under both quasi-static (uniaxial compression) and dynamic (projectile impact) loading conditions (Fig. 5). Notably, the specific strength of our MEA microlattices surpasses most reported micro/nanolattices (Fig. 5A) owing to the high density of dislocation cells induced by our HR-SLM system. While certain microlattices, such as Ti-6Al-4V and SiOC, exhibit comparable or higher specific strengths, they often succumb to catastrophic brittle failure at low strains (typically below 20%). Consequently, these strong yet brittle lattices demonstrate lower specific energy absorption than MEA microlattices, which exhibit both high strength and ductility due to the inherent low SFE of the CoCrNi (Fig. 5B). Intriguingly, contrary to the quasi-static regime where monolithic materials typically outperform cellular structures, the specific inelastic energy values for MEA microlattices surpass those of other monolithic metals/alloys across all tested impact energies (Fig. 5C). The superior energy dissipation performance of the MEA microlattices in the dynamic regime can mainly be attributed to the enhanced inertial response induced by the gyroid shell architecture, elevating the effective dynamic stress in the metamaterial. Consequently, the enhanced dynamic stress results in the early activation of toughening mechanisms in the low SFE MEA, thereby amplifying its strain rate–dependent properties. This underscores the pivotal role of both 3D architecture and HR-SLM–induced dynamic toughening mechanisms in achieving lightweight extreme impact mitigation.

DISCUSSION

In summary, we fabricated 3D CoCrNi MEA microlattices that exhibit ultrahigh-energy dissipation in both the quasi-static and dynamic regimes (covering seven orders of magnitude in strain rates)

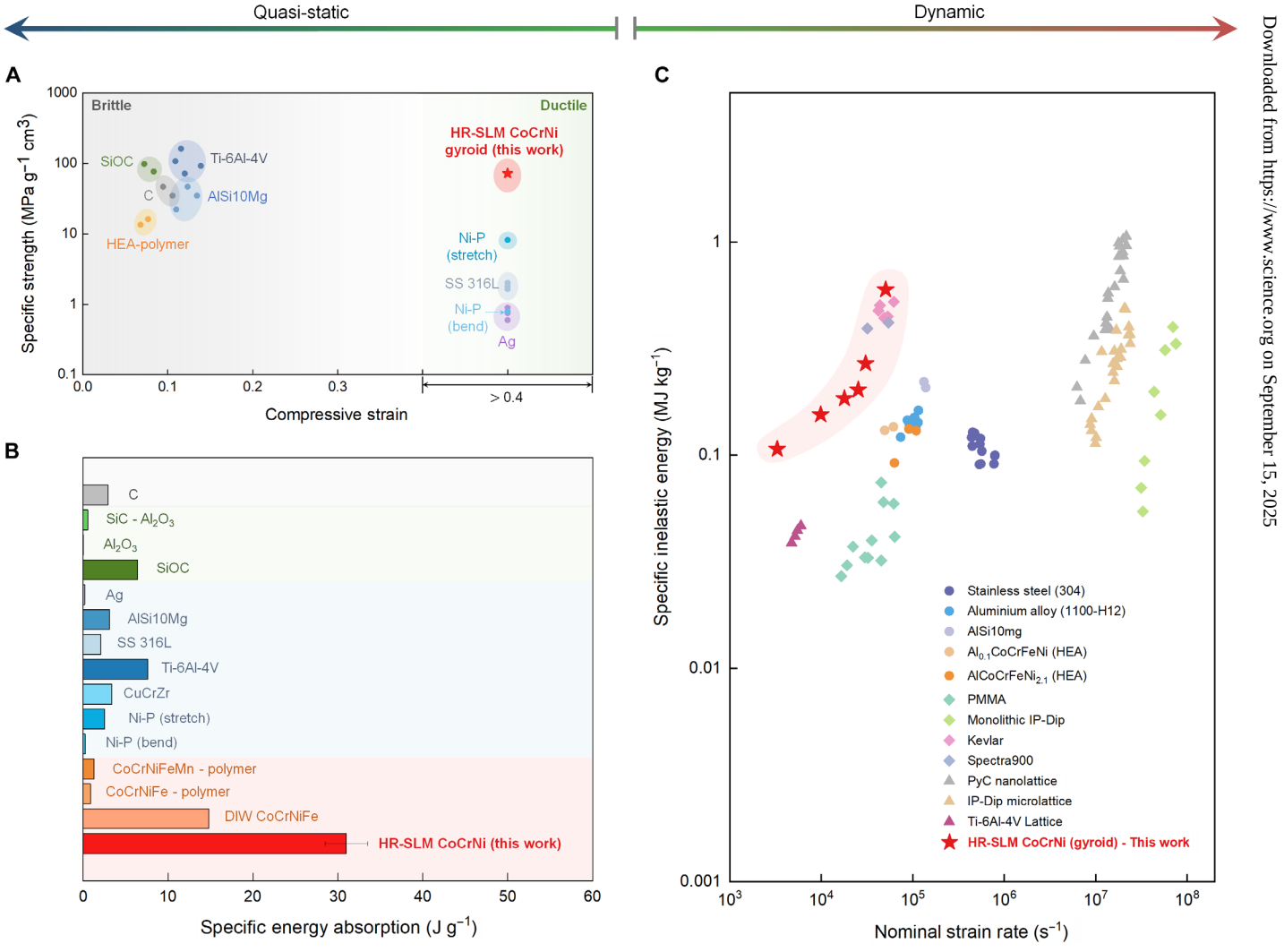

Fig. 5. Quasi-static and dynamic performance comparison of our HR-SLM MEA microlattices against existing micro-architected metamaterials and metals/alloys. (A and B) Plot comparing our MEA microlattices with other existing lattices in terms of its (**A**) specific compressive strength versus maximum strain and (**B**) specific energy absorption. The referenced data were extracted from table S9. (**C**) Plot comparing the specific inelastic energy dissipated of the MEA microlattices against reported metals/alloys upon projectile impact at various impact energies. The referenced data were extracted from table S10.

by using a custom-built HR-SLM system. The synergistic interplay between architectural features, particularly superior in the shell-based architecture compared to truss-based ones, and the intrinsic toughening mechanisms derived from the MEA composition and HR-SLM artifacts resulted in specific energy dissipation surpassing that of reported microlattices and metallic materials.

Specifically, we identified three main design parameters that could aid the community to achieve high-energy dissipation under projectile impact in metallic metamaterials: (i) maximizing self-contact and plastic dissipation in the large strain, compaction regime; (ii) optimizing inertial response to amplify dynamic stress within the metamaterial and enhance strain rate–dependent material properties; and (iii) minimizing SFE to enable a continuous evolution of multiscale deformation mechanisms, which interacts with the high density of dislocation cells induced by the HR-SLM, thereby dissipating energy and prolonging strain hardening behavior across multiple strain rates.

Overall, our study not only provides a pathway for achieving ultrahigh dynamic energy dissipation performance with macroscale sample sizes but also lays the foundation for understanding the intricate relationship between architecture-induced, (manufacturing) process-induced, and material-induced deformation mechanisms in metallic metamaterials. This knowledge opens avenues for inverse design of metamaterials, in particular in tailoring dynamic responses for lightweight crash absorption applications in the defense, aerospace, and automotive sectors.

MATERIALS AND METHODS

Fabrication of MEA samples

A self-developed SLM machine, adapted from the Han's Laser M100μ, was used to produce specimens in this study. Pure CoCrNi MEA powders are provided by Jiu Chun New Material Technology (Suzhou) Co. Ltd., with particle size ranging from 5 to 25 μm. The investigation into the impact of process parameters on roughness, feature size, relative density, and mechanical properties involved the creation of monolithic cuboid and tensile samples. In summary, a comprehensive parameter sweep was executed, varying the power of the laser, hatching distance, and scanning speed and while maintaining a constant slicing distance of 10 μm (see details in text S1). For microhardness testing, bulk samples underwent initial polishing to achieve a surface finish of 3000-grit using SiC paper, followed by a mirror finish using a 0.1-μm colloidal diamond polishing solution. EBSD samples underwent additional polishing through electrochemical means without chemical etching. The electrochemical polishing solution contains nitric acid and ethanol mixed in a 1:4 volume ratio. Electrochemical polishing was conducted at 20 V for 1 min, while the temperature was maintained at −20°C.

Material characterizations

The microstructure and composition of the HR-SLM MEA were examined using field-emission scanning electron microscopy (FESEM), FEI Quanta FEG450, which is equipped with energy dispersive x-ray spectroscopy (EDX) from Oxford Instruments. In addition, TEM using JEOL JEM 2100 and selected-area electron diffraction were used, in which TEM specimens were manufactured by through focused ion beam. EBSD analysis was conducted using a FESEM (FEI Scios) with the Aztec software, and subsequent processing of the EBSD data was carried out using ATEX software. For phase identification, x-ray diffraction, Rigaku SmartLab, using Cu-Kα radiation and a scanning speed of 2° min^{-1} was used.

Mechanical characterizations

Microhardness of the HR-SLM MEA cuboids was obtained by using a microhardness testing machine (Fischer HM2000XY) using a force of 1 N with a constant ramp rate of 50 mN s^{-1} and hold time of 20 s. For the bulk tensile samples and microlattices, in situ, uniaxial tension and compression experiments were performed via an MTS 810 Universal Testing Machine. A digital camera (Canon EOS R5) was used to capture the in situ mechanical response of the microlattices. All tension and compression experiments were conducted at a prescribed strain rate of 10^{-3} s^{-1}. To ensure repeatability, at least four dogbone and microlattice samples were tested for each process condition and architecture, respectively. The compressive stress of the microlattice was calculated by normalizing the force with the nominal area of the cubic lattices. Dynamic impact experiments were executed inside a chamber that holds the microlattice samples, a launch tube which propels the projectile using a gas gun, and a pressurized vessel. The velocity of the striking projectile was managed through the pressurized N_2 gas pressure. A high-speed camera, Photron FASTCAM SA-Z, operating at 60,000 frames per second, was used to monitor the impact process. A Q195 structural carbon steel projectile, measuring 5 mm in diameter and weighing 0.5 g, was used. Analysis of images using PFY4 software allowed for the extraction of key moments in the impact experiment.

Finite element modeling

All finite element simulations were performed using ABAQUS (Simulia). To determine the directional stiffness, computational homogenization was conducted for the BCC, octet, and gyroid architectures using ABAQUS/Standard (Simulia), whereby each architecture was meshed with quadratic tetrahedral elements (C3D10). The intrinsic mechanical properties of the MEA were obtained from tension experiments of printed monolithic MEA samples following ASTM E8 standard geometry (see details in texts S1 and S3 and fig. S6). Periodic boundary conditions were implemented to restrict relative displacements between opposing faces, and linear perturbation was imposed on the unit cells using six strain vectors that are linearly independent. The resultant stress for each case of applied strain was obtained, and the compliance tensor was subsequently formulated. A similar setup using ABAQUS/Standard (Simulia) and C3D10 elements was used for quasi-static uniaxial compression of lattices, except a displacement corresponding to 20% engineering strain was imposed to the top face, while an encastre boundary condition was imposed on the bottom face. The inertial response for each architecture was investigated via dynamic implicit simulations in ABAQUS/Standard (Simulia) with similar meshing parameters. The top face was configured to undergo compression, ensuring a maximum of 5% engineering strain was applied at rates spanning from 1 to 100 s^{-1}. Simultaneously, an encastre boundary condition was implemented on the bottom face. Dynamic explicit simulations using ABAQUS/Explicit with general contact properties were performed to understand the compaction of the lattice architectures upon projectile impact. A maximum displacement corresponding to two times the unit cell size was imposed on the spherical projectile to standardize compaction behavior, and the nominal strain rate applied was 1000 s^{-1}.

Supplementary Materials

The PDF file includes:

Texts S1 to S3
Figs. S1 to S29
Tables S1 to S10
Legends for movies S1 and S2
References

Other Supplementary Material for this manuscript includes the following:

Movies S1 and S2

REFERENCES AND NOTES

1. T. A. Schaedler, W. B. Carter, Architected cellular materials. *Annu. Rev. Mat. Res.* **46**, 187–210 (2016).
2. N. A. Fleck, V. S. Deshpande, M. F. Ashby, Micro-architectured materials: Past, present and future. *Proc. R. Soc.* **466**, 2495–2516 (2010).
3. J. Bauer, L. R. Meza, T. A. Schaedler, R. Schwaiger, X. Zheng, L. Valdevit, Nanolattices: An emerging class of mechanical metamaterials. *Adv. Mater.* **29**, 1701850 (2017).
4. J. U. Surjadi, L. Gao, H. Du, X. Li, X. Xiong, N. X. Fang, Y. Lu, Mechanical metamaterials and their engineering applications. *Adv. Eng. Mater.* **21**, 1800864 (2019).
5. T. A. Schaedler, A. J. Jacobsen, A. Torrents, A. E. Sorensen, J. Lian, J. R. Greer, L. Valdevit, W. B. Carter, Ultralight metallic microlattices. *Science* **334**, 962–965 (2011).
6. X. Zheng, H. Lee, T. H. Weisgraber, M. Shusteff, J. DeOtte, E. B. Duoss, J. D. Kuntz, M. M. Biener, Q. Ge, J. A. Jackson, S. O. Kucheyev, N. X. Fang, C. M. Spadaccini, Ultralight, ultrastiff mechanical metamaterials. *Science* **344**, 1373–1377 (2014).
7. X. W. Gu, J. R. Greer, Ultra-strong architected Cu meso-lattices. *Extreme Mech. Lett.* **2**, 7–14 (2015).
8. X. Zheng, W. Smith, J. Jackson, B. Moran, H. Cui, D. Chen, J. Ye, N. Fang, N. Rodriguez, T. Weisgraber, C. M. Spadaccini, Multiscale metallic metamaterials. *Nat. Mater.* **15**, 1100–1106 (2016).
9. M. A. Saccone, R. A. Gallivan, K. Narita, D. W. Yee, J. R. Greer, Additive manufacturing of micro-architected metals via hydrogel infusion. *Nature* **612**, 685–690 (2022).
10. R. A. W. Mines, S. Tsopanos, Y. Shen, R. Hasan, S. McKown, Drop weight impact behaviour of sandwich panels with metallic micro lattice cores. *Int. J. Impact Eng.* **60**, 120–132 (2013).
11. S. Shan, S. H. Kang, J. R. Raney, P. Wang, L. Fang, F. Candido, J. A. Lewis, K. Bertoldi, Multistable architected materials for trapping elastic strain energy. *Adv. Mater.* **27**, 4296–4301 (2015).
12. T. Tancogne-Dejean, A. B. Spierings, D. Mohr, Additively-manufactured metallic micro-lattice materials for high specific energy absorption under static and dynamic loading. *Acta Mater.* **116**, 14–28 (2016).
13. J. A. Hawreliak, J. Lind, B. Maddox, M. Barham, M. Messner, N. Barton, B. J. Jensen, M. Kumar, Dynamic behavior of engineered lattice materials. *Sci. Rep.* **6**, 28094 (2016).
14. T. Tancogne-Dejean, X. Li, M. Diamantopoulou, C. C. Roth, D. Mohr, High strain rate response of additively-manufactured plate-lattices: Experiments and modeling. *J. Dyn. Behav. Mater.* **5**, 361–375 (2019).
15. C. M. Portela, B. W. Edwards, D. Veysset, Y. Sun, K. A. Nelson, D. M. Kochmann, J. R. Greer, Supersonic impact resilience of nanoarchitected carbon. *Nat. Mater.* **20**, 1491–1497 (2021).
16. E. P. George, D. Raabe, R. O. Ritchie, High-entropy alloys. *Nat. Rev. Mater.* **4**, 515–534 (2019).
17. B. Gludovatz, A. Hohenwarter, K. V. S. Thurston, H. Bei, Z. Wu, E. P. George, R. O. Ritchie, Exceptional damage-tolerance of a medium-entropy alloy CrCoNi at cryogenic temperatures. *Nat. Commun.* **7**, 10602 (2016).
18. S. Zhao, S. Yin, X. Liang, F. Cao, Q. Yu, R. Zhang, L. Dai, C. J. Ruestes, R. O. Ritchie, A. M. Minor, Deformation and failure of the CrCoNi medium-entropy alloy subjected to extreme shock loading. *Sci. Adv.* **9**, eadf8602 (2023).
19. L. Gao, J. Song, Z. Jiao, W. Liao, J. Luan, J. U. Surjadi, J. Li, H. Zhang, D. Sun, C. T. Liu, Y. Lu, High-entropy alloy (HEA)-coated nanolattice structures and their mechanical properties. *Adv. Eng. Mater.* **20**, 1700625 (2018).
20. X. Zhang, J. Yao, B. Liu, J. Yan, L. Lu, Y. Li, H. Gao, X. Li, Three-dimensional high-entropy alloy–polymer composite nanolattices that overcome the strength–recoverability trade-off. *Nano Lett.* **18**, 4247–4256 (2018).
21. X. Feng, J. U. Surjadi, R. Fan, X. Li, W. Zhou, S. Zhao, Y. Lu, Microalloyed medium-entropy alloy (MEA) composite nanolattices with ultrahigh toughness and cyclability. *Mater. Today* **42**, 10–16 (2021).
22. J. U. Surjadi, X. Feng, R. Fan, W. Lin, X. Li, Y. Lu, Hollow medium-entropy alloy nanolattices with ultrahigh energy absorption and resilience. *NPG Asia Mater.* **13**, 36 (2021).
23. J. U. Surjadi, X. Feng, W. Zhou, Y. Lu, Optimizing film thickness to delay strut fracture in high-entropy alloy composite microlattices. *Inter. J. Extrem. Manuf.* **3**, 025101 (2021).
24. C. Kenel, N. P. M. Casati, D. C. Dunand, 3D ink-extrusion additive manufacturing of CoCrFeNi high-entropy alloy micro-lattices. *Nat. Commun.* **10**, 904 (2019).
25. S. Peng, S. Mooraj, R. Feng, L. Liu, J. Ren, Y. Liu, F. Kong, Z. Xiao, C. Zhu, P. K. Liaw, W. Chen, Additive manufacturing of three-dimensional (3D)-architected CoCrFeNiMn high-entropy alloy with great energy absorption. *Scr. Mater.* **190**, 46–51 (2021).
26. Y. M. Wang, T. Voisin, J. T. McKeown, J. Ye, N. P. Calta, Z. Li, Z. Zeng, Y. Zhang, W. Chen, T. T. Roehling, R. T. Ott, M. K. Santala, P. J. Depond, M. J. Matthews, A. V. Hamza, T. Zhu, Additively manufactured hierarchical stainless steels with high strength and ductility. *Nat. Mater.* **17**, 63–71 (2018).
27. V. S. Deshpande, N. A. Fleck, M. F. Ashby, Effective properties of the octet-truss lattice material. *J. Mechanic. Phys. Solids* **49**, 1747–1769 (2001).
28. O. Al-Ketan, R. Rezgui, R. Rowshan, H. Du, N. X. Fang, R. K. Abu Al-Rub, Microarchitected stretching-dominated mechanical metamaterials with minimal surface topologies. *Adv. Eng. Mater.* **20**, 1800029 (2018).
29. Y. Jiang, Q. Wang, Highly-stretchable 3D-architected mechanical metamaterials. *Sci. Rep.* **6**, 34147 (2016).
30. Q. Sun, J. Sun, K. Guo, L. Wang, Compressive mechanical properties and energy absorption characteristics of SLM fabricated Ti6Al4V triply periodic minimal surface cellular structures. *Mech. Mater.* **166**, 104241 (2022).
31. T. Butruille, J. C. Crone, C. M. Portela, Decoupling particle-impact dissipation mechanisms in 3D architected materials. *Proc. Natl. Acad. Sci. U.S.A.* **121**, e2313962121 (2024).
32. A. T. Barnes, K. Ravi-Chandar, S. Kyriakides, S. Gaitanaros, Dynamic crushing of aluminum foams: Part I – Experiments. *Int. J. Solids Struct.* **51**, 1631–1645 (2014).
33. J. S. Weeks, G. Ravichandran, High strain-rate compression behavior of polymeric rod and plate Kelvin lattice structures. *Mech. Mater.* **166**, 104216 (2022).
34. Z. Ghasemi, T. dos Santos, J. A. Rodríguez-Martínez, A. Srivastava, Inertial effect on dynamic hardness and apparent strain-rate sensitivity of ductile materials. *J. Mech. Phys. Solids* **180**, 105418 (2023).
35. S. Zhao, Z. Li, C. Zhu, W. Yang, Z. Zhang, D. E. J. Armstrong, P. S. Grant, R. O. Ritchie, M. A. Meyers, Amorphization in extreme deformation of the CrMnFeCoNi high-entropy alloy. *Sci. Adv.* **7**, eabb3108 (2021).
36. Y. L. Li, D. Yao, Z. W. Liu, J. C. Luo, H. W. Qiao, L. Sun, X. S. Jiang, P. Z. Li, The ductile-brittle transition mechanism of 15MnTi steel under dynamic loading. *Strength Mater.* **55**, 653–671 (2023).
37. Y. Tang, R. Wang, B. Xiao, Z. Zhang, S. Li, J. Qiao, S. Bai, Y. Zhang, P. K. Liaw, A review on the dynamic-mechanical behaviors of high-entropy alloys. *Prog. Mater. Sci.* **135**, 101090 (2023).
38. J. Ren, Y. Zhang, D. Zhao, Y. Chen, S. Guan, Y. Liu, L. Liu, S. Peng, F. Kong, J. D. Poplawsky, G. Gao, T. Voisin, K. An, Y. M. Wang, K. Y. Xie, T. Zhu, W. Chen, Strong yet ductile nanolamellar high-entropy alloys by additive manufacturing. *Nature* **608**, 62–68 (2022).
39. T. Song, Z. Chen, X. Cui, S. Lu, H. Chen, H. Wang, T. Dong, B. Qin, K. C. Chan, M. Brandt, X. Liao, S. P. Ringer, M. Qian, Strong and ductile titanium–oxygen–iron alloys by additive manufacturing. *Nature* **618**, 63–68 (2023).
40. T. Zhang, Z. Huang, T. Yang, H. Kong, J. Luan, A. Wang, D. Wang, W. Kuo, Y. Wang, C.-T. Liu, In situ design of advanced titanium alloy with concentration modulations by additive manufacturing. *Science* **374**, 478–482 (2021).
41. G. Laplanche, A. Kostka, C. Reinhart, J. Hunfeld, G. Eggeler, E. P. George, Reasons for the superior mechanical properties of medium-entropy CrCoNi compared to high-entropy CrMnFeCoNi. *Acta Mater.* **128**, 292–303 (2017).
42. A. J. Birnbaum, J. C. Steuben, E. J. Barrick, A. P. Iliopoulos, J. G. Michopoulos, Intrinsic strain aging, Σ3 boundaries, and origins of cellular substructure in additively manufactured 316L. *Addit. Manuf.* **29**, 100784 (2019).
43. D. Kong, C. Dong, S. Wei, X. Ni, L. Zhang, R. Li, L. Wang, C. Man, X. Li, About metastable cellular structure in additively manufactured austenitic stainless steels. *Addit. Manuf.* **38**, 101804 (2021).
44. L. Liu, Q. Ding, Y. Zhong, J. Zou, J. Wu, Y.-L. Chiu, J. Li, Z. Zhang, Q. Yu, Z. Shen, Dislocation network in additive manufactured steel breaks strength–ductility trade-off. *Mater. Today* **21**, 354–361 (2018).
45. Z. Li, Y. Cui, W. Yan, D. Zhang, Y. Fang, Y. Chen, Q. Yu, G. Wang, H. Ouyang, C. Fan, Q. Guo, D. B. Xiong, S. Jin, G. Sha, N. Ghoniem, Z. Zhang, Y. M. Wang, Enhanced strengthening and hardening via self-stabilized dislocation network in additively manufactured metals. *Mater. Today* **50**, 79–88 (2021).
46. Q. Pan, L. Zhang, R. Feng, Q. Lu, K. An, A. C. Chuang, J. D. Poplawsky, P. K. Liaw, L. Lu, Gradient cell–structured high-entropy alloy with exceptional strength and ductility. *Science* **374**, 984–989 (2021).
47. Z. Zhang, H. Sheng, Z. Wang, B. Gludovatz, Z. Zhang, E. P. George, Q. Yu, S. X. Mao, R. O. Ritchie, Dislocation mechanisms and 3D twin architectures generate exceptional strength-ductility-toughness combination in CrCoNi medium-entropy alloy. *Nat. Commun.* **8**, 14390 (2017).
48. G. Wu, C. Liu, L. Sun, Q. Wang, B. Sun, B. Han, J.-J. Kai, J. Luan, C. T. Liu, K. Cao, Y. Lu, L. Cheng, J. Lu, Hierarchical nanostructured aluminum alloy with ultrahigh strength and large plasticity. *Nat. Commun.* **10**, 5099 (2019).

49. K. Jiang, J. Li, X. Kan, F. Zhao, B. Hou, Q. Wei, T. Suo, Adiabatic shear localization induced by dynamic recrystallization in an FCC high entropy alloy. *Int. J. Plast.* **162**, 103550 (2023).
50. Z. Li, S. Zhao, S. M. Alotaibi, Y. Liu, B. Wang, M. A. Meyers, Adiabatic shear localization in the CrMnFeCoNi high-entropy alloy. *Acta Mater.* **151**, 424–431 (2018).
51. P. J. Noell, R. B. Sills, A. A. Benzerga, B. L. Boyce, Void nucleation during ductile rupture of metals: A review. *Prog. Mater. Sci.* **135**, 101085 (2023).
52. ASTM, Standard test methods for tension testing of metallic materials. *Annual Book of ASTM Standards* (ASTM, 2001).
53. S. Qu, J. Ding, J. Fu, M. Fu, B. Zhang, X. Song, High-precision laser powder bed fusion processing of pure copper. *Addit. Manuf.* **48**, 102417 (2021).
54. J. Fu, S. Qu, J. Ding, X. Song, M. W. Fu, Comparison of the microstructure, mechanical properties and distortion of stainless steel 316L fabricated by micro and conventional laser powder bed fusion. *Addit. Manuf.* **44**, 102067 (2021).
55. K. E. Puttick, Ductile fracture in metals. *Philos. Mag.* **4**, 964–969 (1959).
56. V. Tvergaard, A. Needleman, Analysis of the cup-cone fracture in a round tensile bar. *Acta Metall.* **32**, 157–169 (1984).
57. T. Voisin, J.-B. Forien, A. Perron, S. Aubry, N. Bertin, A. Samanta, A. Baker, Y. M. Wang, New insights on cellular structures strengthening mechanisms and thermal stability of an austenitic stainless steel fabricated by laser powder-bed-fusion. *Acta Mater.* **203**, 116476 (2021).
58. B. B. He, B. Hu, H. W. Yen, G. J. Cheng, Z. K. Wang, H. W. Luo, M. X. Huang, High dislocation density–Induced large ductility in deformed and partitioned steels. *Science* **357**, 1029–1032 (2017).
59. D. Lin, L. Xu, H. Jing, Y. Han, L. Zhao, F. Minami, Effects of annealing on the structure and mechanical properties of FeCoCrNi high-entropy alloy fabricated via selective laser melting. *Addit. Manuf.* **32**, 101058 (2020).
60. Y. S. Kim, H. Chae, W. Woo, D.-K. Kim, D.-H. Lee, S. Harjo, T. Kawasaki, S. Y. Lee, Multiple deformation scheme in direct energy deposited CoCrNi medium entropy alloy at 210K. *Mater. Sci. Eng. A Struct.Mater* **828**, 142059 (2021).
61. G. I. Taylor, The mechanism of plastic deformation of crystals. Part I.—Theoretical. *Proc. R. Soc. Lond. A* **145**, 362–387 (1934).
62. Z. G. Zhu, Q. B. Nguyen, F. L. Ng, X. H. An, X. Z. Liao, P. K. Liaw, S. M. L. Nai, J. Wei, Hierarchical microstructure and strengthening mechanisms of a CoCrFeNiMn high entropy alloy additively manufactured by selective laser melting. *Scr. Mater.* **154**, 20–24 (2018).
63. H. Jung, J. Lee, G. H. Gu, H. Lee, S.-M. Seo, A. Zargaran, H. S. Kim, S. S. Sohn, Multiscale defects enable synergetic improvement in yield strength of CrCoNi-based medium-entropy alloy fabricated via laser-powder bed fusion. *Addit. Manuf.* **61**, 103360 (2023).
64. M. Yi, J. Tu, L. Yang, Z. Zhou, S. Chen, L. Ding, Y. Du, Y. Qiu, Y. Liang, Microstructural mechanisms endowing high strength-ductility synergy in CoCrNi medium entropy alloy prepared by laser powder bed fusion. *Addit. Manuf.* **87**, 104229 (2024).
65. C. Pan, D. Zhu, H. Luo, K. Kosiba, S. Qu, C. Yang, X. Li, Fabrication of high-performance CoCrNi medium entropy alloy by laser powder bed fusion: The effect of grain boundary segregation. *Compos. B Eng.* **253**, 110540 (2023).
66. S. B. A. Malladi, D. Riabov, S. Guo, L. Nyborg, Additive manufacturing of interstitial nitrogen-strengthened CoCrNi medium entropy alloy. *Adv. Eng. Mater.* **26**, 2401182 (2024).
67. W. Woo, Y. Kim, H. Chae, S. Lee, J. Jeong, C. Lee, J. Won, Y. Na, T. Kawasaki, S. Harjo, K. An, Competitive strengthening between dislocation slip and twinning in cast-wrought and additively manufactured CrCoNi medium entropy alloys. *Acta Mater.* **246**, 118699 (2023).
68. Y. Chew, G. J. Bi, Z. G. Zhu, F. L. Ng, F. Weng, S. B. Liu, S. M. L. Nai, B. Y. Lee, Microstructure and enhanced strength of laser aided additive manufactured CoCrFeNiMn high entropy alloy. *Mater. Sci. Eng. A* **744**, 137–144 (2019).
69. S. Xiang, H. Luan, J. Wu, K.-F. Yao, J. Li, X. Liu, Y. Tian, W. Mao, H. Bai, G. Le, Q. Li, Microstructures and mechanical properties of CrMnFeCoNi high entropy alloys fabricated using laser metal deposition technique. *J. Alloys Compd.* **773**, 387–392 (2019).
70. Z. Tong, X. Ren, J. Jiao, W. Zhou, Y. Ren, Y. Ye, E. A. Larson, J. Gu, Laser additive manufacturing of FeCrCoMnNi high-entropy alloy: Effect of heat treatment on microstructure, residual stress and mechanical property. *J. Alloys Compd.* **785**, 1144–1159 (2019).
71. S. Guan, D. Wan, K. Solberg, F. Berto, T. Welo, T. M. Yue, K. C. Chan, Additive manufacturing of fine-grained and dislocation-populated CrMnFeCoNi high entropy alloy by laser engineered net shaping. *Mater. Sci. Eng. A* **761**, 138056 (2019).
72. M. A. Melia, J. D. Carroll, S. R. Whetten, S. N. Esmaeely, J. Locke, E. White, I. Anderson, M. Chandross, J. R. Michael, N. Argibay, E. J. Schindelholz, A. B. Kustas, Mechanical and corrosion properties of additively manufactured CoCrFeMnNi high entropy alloy. *Addit. Manuf.* **29**, 100833 (2019).
73. J. Joseph, N. Stanford, P. Hodgson, D. M. Fabijanic, Tension/compression asymmetry in additive manufactured face centered cubic high entropy alloy. *Scr. Mater.* **129**, 30–34 (2017).
74. J. Joseph, P. Hodgson, T. Jarvis, X. Wu, N. Stanford, D. M. Fabijanic, Effect of hot isostatic pressing on the microstructure and mechanical properties of additive manufactured Al_xCoCrFeNi high entropy alloys. *Mater. Sci. Eng. A* **733**, 59–70 (2018).
75. P. F. Zhou, D. H. Xiao, Z. Wu, X. Q. Ou, $Al_{0.5}$FeCoCrNi high entropy alloy prepared by selective laser melting with gas-atomized pre-alloy powders. *Mater. Sci. Eng. A* **739**, 86–89 (2019).
76. Y. Brif, M. Thomas, I. Todd, The use of high-entropy alloys in additive manufacturing. *Scr. Mater.* **99**, 93–96 (2015).
77. Z. Sun, X. P. Tan, M. Descoins, D. Mangelinck, S. B. Tor, C. S. Lim, Revealing hot tearing mechanism for an additively manufactured high-entropy alloy via selective laser melting. *Scr. Mater.* **168**, 129–133 (2019).
78. R. Li, P. Niu, T. Yuan, P. Cao, C. Chen, K. Zhou, Selective laser melting of an equiatomic CoCrFeMnNi high-entropy alloy: Processability, non-equilibrium microstructure and mechanical property. *J. Alloys Compd.* **746**, 125–134 (2018).
79. R. Zhou, Y. Liu, C. Zhou, S. Li, W. Wu, M. Song, B. Liu, X. Liang, P. K. Liaw, Microstructures and mechanical properties of C-containing FeCoCrNi high-entropy alloy fabricated by selective laser melting. *Intermetallics* **94**, 165–171 (2018).
80. W. Wu, R. Zhou, B. Wei, S. Ni, Y. Liu, M. Song, Nanosized precipitates and dislocation networks reinforced C-containing CoCrFeNi high-entropy alloy fabricated by selective laser melting. *Mater Charact* **144**, 605–610 (2018).
81. T. Fujieda, M. Chen, H. Shiratori, K. Kuwabara, K. Yamanaka, Y. Koizumi, A. Chiba, S. Watanabe, Mechanical and corrosion properties of CoCrFeNiTi-based high-entropy alloy additive manufactured using selective laser melting. *Addit. Manuf.* **25**, 412–420 (2019).
82. X. Yang, Y. Zhou, S. Xi, Z. Chen, P. Wei, C. He, T. Li, Y. Gao, H. Wu, Additively manufactured fine grained $Ni_6Cr_4WFe_9Ti$ high entropy alloys with high strength and ductility. *Mater. Sci. Eng. A* **767**, 138394 (2019).
83. K. Kuwabara, H. Shiratori, T. Fujieda, K. Yamanaka, Y. Koizumi, A. Chiba, Mechanical and corrosion properties of AlCoCrFeNi high-entropy alloy fabricated with selective electron beam melting. *Addit. Manuf.* **23**, 264–271 (2018).
84. P. Wang, P. Huang, F. L. Ng, W. J. Sin, S. Lu, M. L. S. Nai, Z. Dong, J. Wei, Additively manufactured CoCrFeNiMn high-entropy alloy via pre-alloyed powder. *Mater. Des.* **168**, 107576 (2019).
85. J. Y. He, W. H. Liu, H. Wang, Y. Wu, X. J. Liu, T. G. Nieh, Z. P. Lu, Effects of Al addition on structural evolution and tensile properties of the FeCoNiCrMn high-entropy alloy system. *Acta Mater.* **62**, 105–113 (2014).
86. J. Wang, S. Niu, T. Guo, H. Kou, J. Li, The FCC to BCC phase transformation kinetics in an $Al_{0.5}$CoCrFeNi high entropy alloy. *J. Alloys Compd.* **710**, 144–150 (2017).
87. Z. Wu, S. A. David, Z. Feng, H. Bei, Weldability of a high entropy CrMnFeCoNi alloy. *Scr. Mater.* **124**, 81–85 (2016).
88. N. Eißmann, B. Klöden, T. Weißgärber, B. Kieback, High-entropy alloy CoCrFeMnNi produced by powder metallurgy. *Powder Metall.* **60**, 184–197 (2017).
89. B. Liu, J. Wang, Y. Liu, Q. Fang, Y. Wu, S. Chen, C. T. Liu, Microstructure and mechanical properties of equimolar FeCoCrNi high entropy alloy prepared via powder extrusion. *Intermetallics* **75**, 25–30 (2016).
90. D. Kong, C. Dong, X. Ni, L. Zhang, J. Yao, C. Man, X. Cheng, K. Xiao, X. Li, Mechanical properties and corrosion behavior of selective laser melted 316L stainless steel after different heat treatment processes. *J. Mater. Sci. Technol.* **35**, 1499–1507 (2019).
91. O. O. Salman, C. Gammer, A. K. Chaubey, J. Eckert, S. Scudino, Effect of heat treatment on microstructure and mechanical properties of 316L steel synthesized by selective laser melting. *Mater. Sci. Eng. A* **748**, 205–212 (2019).
92. N. Chen, G. Ma, W. Zhu, A. Godfrey, Z. Shen, G. Wu, X. Huang, Enhancement of an additive-manufactured austenitic stainless steel by post-manufacture heat-treatment. *Mater. Sci. Eng. A* **759**, 65–69 (2019).
93. A. Riemer, S. Leuders, M. Thöne, H. A. Richard, T. Tröster, T. Niendorf, On the fatigue crack growth behavior in 316L stainless steel manufactured by selective laser melting. *Eng. Fract. Mech.* **120**, 15–25 (2014).
94. K. Chen, D. J. Huang, H. Li, N. Jia, W. Chong, Avoiding abnormal grain growth when annealing selective laser melted pure titanium by promoting nucleation. *Scr. Mater.* **209**, 114377 (2022).
95. M. Wang, B. Song, Q. Wei, Y. Zhang, Y. Shi, Effects of annealing on the microstructure and mechanical properties of selective laser melted AlSi7Mg alloy. *Mater. Sci. Eng. A* **739**, 463–472 (2019).
96. K. Saeidi, L. Kvetková, F. Lofaj, Z. Shen, Austenitic stainless steel strengthened by the in situ formation of oxide nanoinclusions. *RSC Adv.* **5**, 20747–20750 (2015).
97. J. U. Surjadi, L. Gao, K. Cao, R. Fan, Y. Lu, Mechanical enhancement of core-shell microlattices through high-entropy alloy coating. *Sci. Rep.* **8**, 5442 (2018).
98. Z. Ma, D. Z. Zhang, F. Liu, J. Jiang, M. Zhao, T. Zhang, Lattice structures of Cu-Cr-Zr copper alloy by selective laser melting: Microstructures, mechanical properties and energy absorption. *Mater. Des.* **187**, 108406 (2020).
99. E. Hernández-Nava, C. J. Smith, F. Derguti, S. Tammas-Williams, F. Léonard, P. J. Withers, I. Todd, R. Goodall, The effect of defects on the mechanical response of Ti-6Al-4V cubic lattice structures fabricated by electron beam melting. *Acta Mater.* **108**, 279–292 (2016).

100. S. Tsopanos, R. A. W. Mines, S. Mckown, Y. Shen, W. J. Cantwell, W. Brooks, C. J. Sutcliffe, The influence of processing parameters on the mechanical properties of selectively laser melted stainless steel microlattice structures. *J. Manuf. Sci. Eng.* **132**, 041011 (2010).
101. C. Yan, L. Hao, A. Hussein, S. L. Bubb, P. Young, D. Raymont, Evaluation of light-weight AlSi10Mg periodic cellular lattice structures fabricated via direct metal laser sintering. *J. Mater. Process. Technol.* **214**, 856–864 (2014).
102. M. S. Saleh, C. Hu, R. Panat, Three-dimensional microarchitected materials and devices using nanoparticle assembly by pointwise spatial printing. *Sci. Adv.* **3**, e1601986 (2017).
103. Z. C. Eckel, C. Zhou, J. H. Martin, A. J. Jacobsen, W. B. Carter, T. A. Schaedler, Additive manufacturing of polymer-derived ceramics. *Science* **351**, 58–62 (2016).
104. X. Y. Yap, I. Seetoh, W. L. Goh, P. Ye, Y. Zhao, Z. Du, C. Q. Lai, C. L. Gan, Mechanical properties and failure behaviour of architected alumina microlattices fabricated by stereolithography 3D printing. *Int. J. Mech. Sci.* **196**, 106285 (2021).
105. H. Mei, R. Zhao, Y. Xia, J. Du, X. Wang, L. Cheng, Ultrahigh strength printed ceramic lattices. *J. Alloys Compd.* **797**, 786–796 (2019).
106. A. J. Jacobsen, S. Mahoney, W. B. Carter, S. Nutt, Vitreous carbon micro-lattice structures. *Carbon* **49**, 1025–1032 (2011).
107. M. Kristoffersen, M. Costas, T. Koenis, V. Brøtan, C. O. Paulsen, T. Børvik, On the ballistic perforation resistance of additive manufactured AlSi10Mg aluminium plates. *Int. J. Impact Eng.* **137**, 103476 (2020).
108. S. Muskeri, D. Choudhuri, P. A. Jannotti, B. E. Schuster, J. T. Lloyd, R. S. Mishra, S. Mukherjee, Ballistic impact response of $Al_{0.1}$CoCrFeNi high-entropy alloy. *Adv. Eng. Mater.* **22**, 2000124 (2020).
109. D. Choudhuri, P. A. Jannotti, S. Muskeri, S. Shukla, S. Gangireddy, S. Mukherjee, B. E. Schuster, J. T. Lloyd, R. S. Mishra, Ballistic response of a FCC-B2 eutectic $AlCoCrFeNi_{2.1}$ high entropy alloy. *J. Dyn. Behav. Mater.* **5**, 495–503 (2019).
110. J. Dean, C. S. Dunleavy, P. M. Brown, T. W. Clyne, Energy absorption during projectile perforation of thin steel plates and the kinetic energy of ejected fragments. *Int. J. Impact Eng.* **36**, 1250–1258 (2009).
111. N. K. Gupta, M. A. Iqbal, G. S. Sekhon, Experimental and numerical studies on the behavior of thin aluminum plates subjected to impact by blunt-and hemispherical-nosed projectiles. *Int. J. Impact Eng.* **32**, 1921–1944 (2006).
112. L. H. Abbud, A. R. A. Talib, F. Mustapha, H. Tawfique, F. A. Najim, Behaviour of transparent material under high velocity impact. *Int. J. Mech. Mater. Eng.* **5**, 123–128 (2010).
113. B. L. Lee, T. F. Walsh, S. T. Won, H. M. Patts, J. W. Song, A. H. Mayer, Penetration failure mechanisms of armor-grade fiber composites under impact. *J. Compos. Mater.* **35**, 1605–1633 (2001).
114. Z. Xie, X. Fu, Q. Zhang, L. Liu, X. Zhu, Y. Ren, W. Chen, Ballistic performance of additive manufacturing metal lattice structures. *Thin Walled Struct.* **208**, 112763 (2025).

Acknowledgments

Funding: This work was supported by the Hong Kong Research Grants Council Collaborative Research Fund no. C7074-23G (L.W., X.S., and Y.L.), Hong Kong Research Grants Council General Research Fund no. 11200623 (L.W. and Y.L.), Hong Kong Institute for Advanced Study (J.U.S).

Author contributions: Conceptualization: J.U.S., L.W., and Y.L. Data curation: J.U.S., L.W., and B.F.G.A. Formal analysis: J.U.S., L.W., J.D., and X.Z. Funding acquisition: X.S. and Y.L. Investigation: J.U.S., L.W., S.Q., B.F.G.A., X.Z., R.F., Q.Z., and Y.L. Methodology: J.U.S., L.W., S.Q., J.D., B.F.G.A., H.Y., and Y.L. Project administration: J.U.S., X.S., and Y.L. Resources: L.W., Q.Z., X.S., and Y.L. Software: J.U.S., L.W., and J.D. Supervision: Q.Z., X.S., and Y.L. Validation: J.U.S., L.W., and S.Q. Visualization: J.U.S. and L.W. Writing–original draft: J.U.S. and L.W. Writing–review and editing: J.U.S., L.W., S.Q., J.D., X.S., and Y.L. **Competing interests:** The authors declare that they have no competing interests. **Data and materials availability:** All data needed to evaluate the conclusions in the paper are present in the paper and/or the Supplementary Materials.

Submitted 9 September 2024
Accepted 8 April 2025
Published 7 May 2025
10.1126/sciadv.adt0589